X-ray spectroscopy of merging galaxy clusters

Urdampilleta Aldema, I.

1 Introduction

1.1 Galaxy clusters

Galaxy clusters are the largest virialized objects in the Universe, which lay at the nodes of the cosmic web. Clusters contain between a hundred to a thousand of galaxies, who include only $\sim$5% of the total mass, $\sim 10^{14}$–10^{15} $M_{\odot}$. These galaxies are embedded in hot (10^{7}–10^{8} K or 1–10 keV) ionized gas, known as the intracluster medium (ICM), which has a significant contribution to the baryonic component and constitutes $\sim$15% of the mass budget. The rest of the mass, $\sim$80%, is dominated by dark matter (e.g. Blumenthal et al. 1984; Sanderson et al. 2003; Vikhlinin et al. 2006). The ICM is a low density plasma ($\sim 10^{-4}$–10^{-3} cm^{-3}) observed in X-rays by measuring its thermal plasma emission (Mitchell et al. 1976; Serlemitsos et al. 1977; Forman & Jones 1982).

Galaxy clusters can be observed not only using X-rays, but also other wavelengths such as optical, infrared, radio and using techniques such as the Sunyaev-Zel'dovich effect or gravitational lensing, see Fig. 1.1. Each of them provides a distinct kind of information about the cluster. Optical light, for example, shows the individual galaxies of the clusters and their overdensities at a similar redshift. X-rays are emitted by the diffuse hot plasma in the ICM, and radio emission traces cosmic rays, magnetic fields and discrete radio sources found in clusters. Moreover, gravitational lensing uses the observed distortions of the galaxies orientation behind the clusters to model the distribution of dark matter and to obtain the cluster masses. Finally, observing the Sunyaev-Zel'dovich effect (distortions of the cosmic microwave background) the density perturbations of the hot plasma can be detected.

Using these techniques the dynamical state of the clusters can be determined as well. They can be either dynamically relaxed or cool-core (CC) clusters, dynamically disturbed or non-cool-core (NCC) clusters and extremely disturbed systems known as merging galaxy clusters.

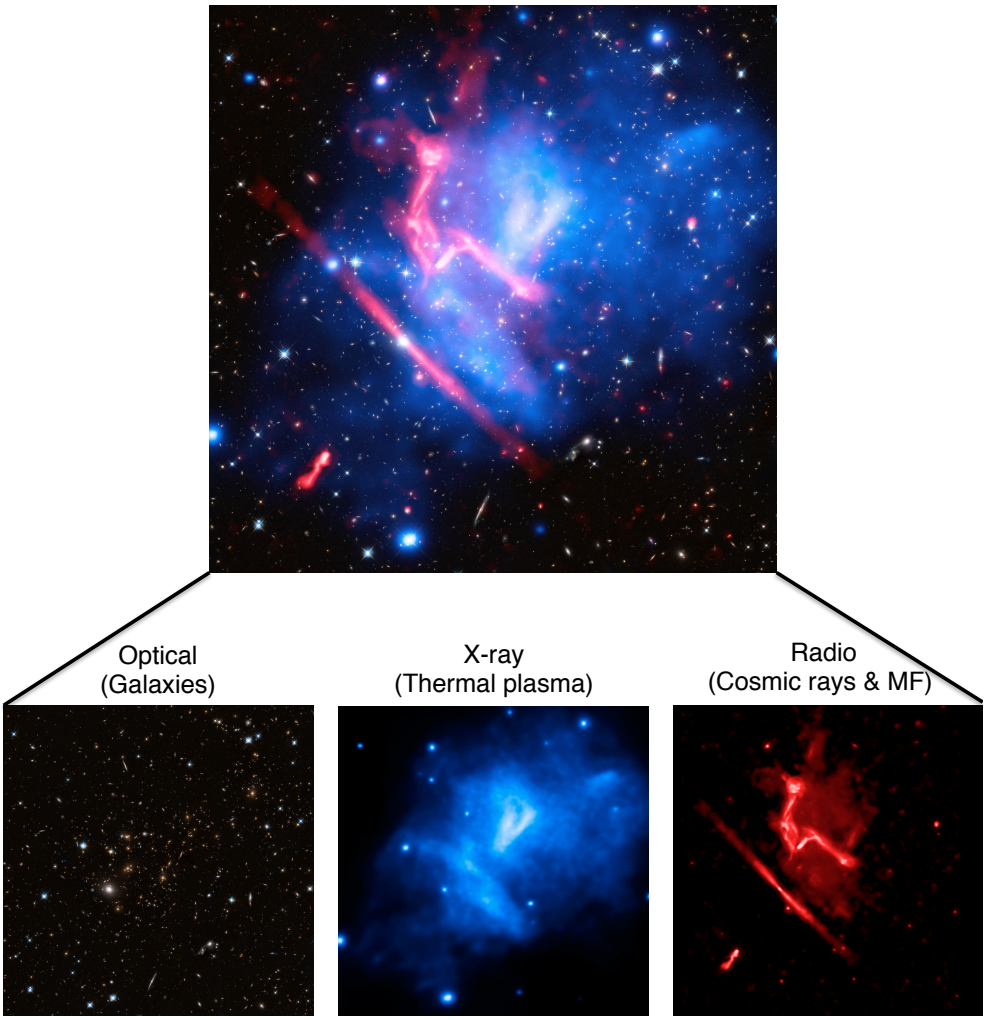

Figure 1.1: The galaxy cluster MACS J0717.5+3745. *Top panel*: Composite image (optical, X-ray and radio) of MACS J0717.5+3745. *Bottom panel*: The *left* panel presents an optical view of the cluster observed with the Hubble Space Telescope (red, green, and blue). In the *middle* panel, the X-ray emission from the thermal ICM is shown in blue using *Chandra* in the 0.5–2.0 keV band (van Weeren et al. 2017). The *right* panel displays the radio emission in red, data from the Jansky Very Large Array (JVLA). (Credit: X-ray: NASA/CXC/SAO/van Weeren et al.; Optical: NASA/STScI; Radio: NRAO/AUI/NSF).

In the CC clusters the central density is high enough to cause a radiative cooling flow on short cosmic timescales. Without any heating mechanism, the temperature in the central region could drop further and form stars (for a review, see Fabian 1994). However, the amount of cool gas found is less than expected (Peterson et al. 2001; Tamura et al. 2001; Kaastra et al. 2001). This suggests that a central source of heating, for example the feedback of an active galactic nucleus (AGN) in the core of the brightest cluster galaxy (BCG), can balance the radiative losses. The CC clusters also show a relatively high central metallicity peak anti-correlated with a low-entropy regime, which will be described in Section 1.3. On the contrary, the NCC clusters show a moderate central abundance peak and higher-entropy profiles.

1.2 Merging Galaxy Clusters

Galaxy clusters are not static entities, they grow hierarchically by the accretion of galaxy filaments (WHIM, warm-hot intergalactic medium) and merging of the surrounding galaxy groups and subclusters. Cluster mergers are the most energetic ($\sim 10^{64}$ erg) events in the Universe since the Big Bang. During these energetic processes (see Fig. 1.2 for a simulation of the Abell 3376 merging process[1]), the ICM of the corresponding (sub)clusters collides and becomes turbulent. Large amounts of thermal (X-ray) and non-thermal (radio) energy are released, giving rise to large scale structures known as shock fronts, cold fronts and turbulence (Markevitch & Vikhlinin 2007). Merger shocks violently compress and heat the X-ray emitting ICM and increase its entropy. In an idealized bimodal merger, "equatorial" shocks form first in the collision region and propagate outwards parallel to the merging axis (see *(c)* panel of Fig. 1.2). After the core passage phase, two shocks move perpendicular to the merging axis, from the center along the hot ICM up to the periphery of the cluster (see *(e)* and *(f)* panels of Fig. 1.2). In some cases, the merger can be violent enough to provoke the core disruption of one (sub)cluster (see *(f)* panel of Fig. 1.2). Cold fronts are also found in mergers and they delimit the boundaries of a cool and dense gas cloud moving through hotter and higher-entropy gas (Vikhlinin et al. 2001). Both, shocks and cold fronts provide a valuable tool to study the physical processes in the ICM at large scales. They can improve the understanding of the dynamical stage of the merger, the gas bulk velocities and their direction of motion.

1.2.1 Shock detection in X-rays

The X-ray shocks produced in a merging cluster show sharp discontinuities between denser and hotter gas in the downstream (post-shock) and more tenuous and cooler gas in the upstream (pre-shock) region. Therefore, temperature and density discontinuities at the same location should be detected to prove the presence of the shocks (see Fig. 1.3). The projected temperatures can be directly inferred from a spectral fit to the spectrum obtained from a selected region in an X-ray observation (see Section 1.4). A proper selection of the post and pre-shock regions is decisive to detect the correct temperature jump value, be-

[1] https://www.youtube.com/watch?v=XYyYIOwdVcw

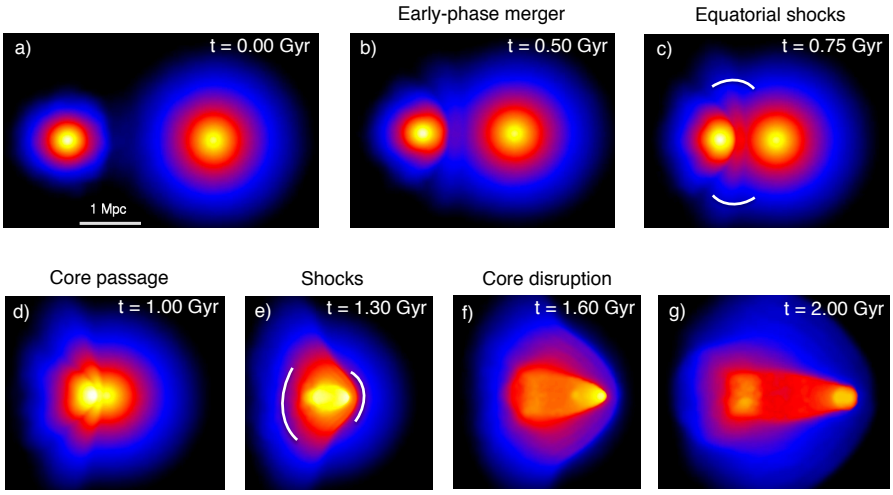

Figure 1.2: Simulation of the merging process of Abell 3376 based on Machado & Lima Neto (2013). *(a)*: Initial scenario with a mass ratio ∼1:6, impact parameter b < 150 kpc and a 1 Mpc separation. *(b)*: Beginning of the collision between the subclusters. *(c)*: Large scale-structures between subclusters and equatorial shocks appear. *(d)*: Beginning of the core passage. *(e)*: Symmetrical shock waves with respect to the center are visible. *(f)*: The core disruption of the most massive cluster has taken place. *(g)*: Late phase of the merging.

cause the post-shock region tends to include a two-temperature structure (mixing of both regions). Meanwhile, the projected density distribution can be derived from the surface brightness (SB) profile assuming spherical symmetry. The SB is frequently described by a broken power-law density profile (Owers et al. 2009; Eckert et al. 2016b):

$$\begin{cases} n_2(r) = n_0 \left(\frac{r}{r_{\rm sh}}\right)^{-\alpha_2} & r \leq r_{\rm sh} \\ \\ n_1(r) = \frac{1}{C} n_0 \left(\frac{r}{r_{\rm sh}}\right)^{-\alpha_1} & r > r_{\rm sh} \end{cases} \tag{1.1}$$

where n_0 is the model density normalization, n is the electron density, C is the compression factor, α_1 and α_2 are the power-law indices, r is the radius from the center, $r_{\rm sh}$ is the shock putative distance and the indices 2 and 1 corresponds to post-shock and pre-shock regions, respectively.

Furthermore, the X-ray shocks can be characterized by the Mach number ($\mathcal{M}_X$) and the shock propagation speeds ($v_{\rm shock} = \mathcal{M}_X \cdot c_{\rm s}$), relative to the pre-shock ICM. $c_{\rm s}$ is the sound speed at the pre-shock regions $c_{\rm s} = \sqrt{\gamma k T_1 / \mu m_p}$ with $\mu = 0.6$. This Mach number is relatively low $\leq$ 3–4 (e.g. Gabici & Blasi 2003; Ryu et al. 2003) and can be assessed from the Rankine-Hugoniot jump condition (Landau & Lifshitz 1959) assuming that all of the dissipated shock energy is thermalized and the ratio of specific heats (the adiabatic

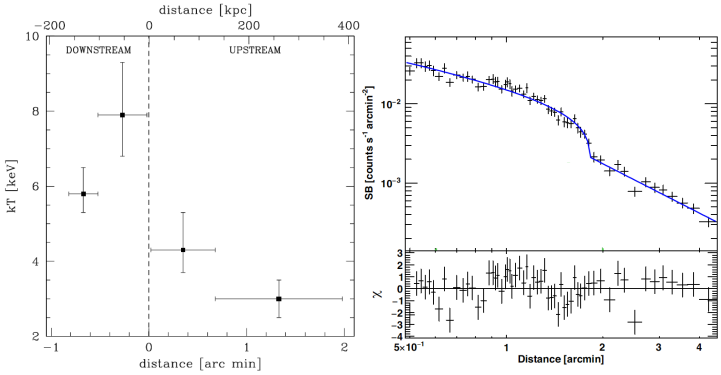

Figure 1.3: *Left panel*: ICM temperature profile across the shock of Abell 115 using *Chandra* observations. The vertical dashed line indicates the tentative shock position derived by the surface brightness discontinuity. *Right panel*: X-ray surface brightness profile in the 0.5-2 keV energy range of Abell 115. Both figures are adopted from Botteon et al. (2016a).

index) is γ = 5/3:

$$\frac{T_2}{T_1} = \frac{5\mathcal{M}_X^4 + 14\mathcal{M}_X^2 - 3}{16\mathcal{M}_X^2}, \tag{1.2}$$

$$\frac{n_2}{n_1} = C = \frac{4\mathcal{M}_X^2}{\mathcal{M}_X^2 + 3}, \tag{1.3}$$

where T is the temperature.

1.2.2 Particle acceleration by shocks

Shocks are thought to (re)accelerate electrons from the thermal distribution up to relativistic energies creating the non-thermal cosmic ray (CR) component of the ICM, by the first-order Fermi diffusive shock acceleration mechanism (hereafter DSA, Drury 1983; Bell 1987; Blandford & Eichler 1987). In the presence of a magnetic field these accelerated electrons can produce extended synchrotron radio emission, inverse Compton (IC) and gamma-ray emission (for a review, see van Weeren et al. 2019). DSA assumes a stationary and continuous injection, which accelerates relativistic CR electrons following a power-law spectrum (for a review, see Feretti et al. 2012):

$$n(E)dE \sim E^{-p}dE, \tag{1.4}$$

with p = 1-2α, where p is the power-law index and α is the radio spectral index for $S_\nu \propto \nu^\alpha$. Diffuse cluster radio sources have usually a step spectral index $\alpha \lesssim$ -1.

The Mach number can be also inferred from the radio observations assuming the simple DSA theory as:

$$\mathcal{M}_R^2 = \frac{2\alpha - 3}{2\alpha + 1}. \tag{1.5}$$

This method and the Rankine-Hugoniot jump condition are a priori independent. Therefore for the same source, if the assumptions are correct, the Mach number derived from these two different wavelength bands should agree with each other.

Recent studies have suggested that the acceleration efficiency of the DSA is low for shocks with $\mathcal{M}$ < 10 and might not be sufficient to produce the observed radio spectral indices (Kang et al. 2012; Pinzke et al. 2013). Nowadays alternative scenarios for the CR acceleration have been proposed as the electron re-acceleration by turbulence (Fujita et al. 2015; Kang 2017), the re-acceleration of pre-existing cosmic ray electrons (Markevitch et al. 2005; Kang et al. 2012; Fujita et al. 2015; Fujita et al. 2016; Kang 2017) or shock drift acceleration (Guo et al. 2014a,b, 2017). They are based on distinct acceleration mechanisms, such as second order Fermi acceleration (Fermi-II), where particles scatter from magnetic inhomogeneities, adiabatic compression or secondary models, where CRe are produced by secondary process.

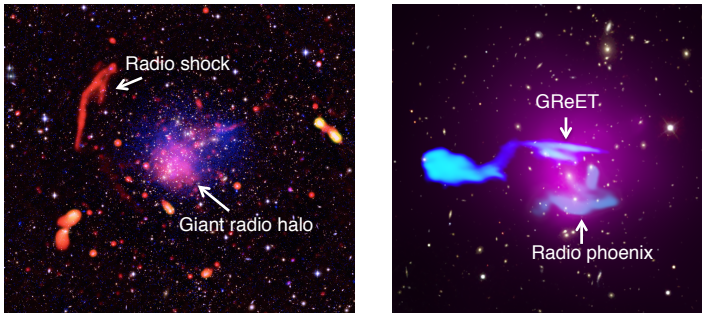

Figure 1.4: *Left panel*: Radio shock and giant radio halo in Abell 2744. The radio features emission in red, data from the Jansky Very Large Array (JVLA), X-ray data from *Chandra* (blue), optical data from *Subaru* and the VLT (red, green and blue). Credit: X-ray: NASA/CXC/ITA/INAF/Merten et al. (2011); Radio: NRAO/AUI/NSF/B. Saxton; Optical: NAOJ/Subaru & ESO/VLT. *Right panel*: GReET and radio phoenix in Abell 1033. Radio emission in blue are data from LOFAR, X-rays from *Chandra* in purple and SDSS optical data. Credit: X-ray: NASA/CXC/Leiden Univ./De Gasperin et al. (2017); Optical: SDSS; Radio: LOFAR/ASTRON, NCRA/TIFR/GMRT.

van Weeren et al. (2019) present a new classification of diffuse radio sources, which includes cluster radio shocks, revived AGN fossil plasma sources, phoenices and GReETs (Gently re-energized tails), and radio halos. The first two ones are thought to trace X-ray shocks:

- **Cluster radio shocks (radio relics)**: Extended diffuse radio sources form by the X-ray shocks (re)acceleration of energetic particles, in the presence of a magnetic field (for a review, see Ferrari et al. 2008; Brunetti & Jones 2014; van Weeren et al. 2019). They are Mpc-size elongated, filamentary and polarized radio structures located usually in the cluster outskirts. The spectral index varies between -1.5 < α < -1.1 and can steepen across the radio shock towards the cluster center. In most of the cases they are associated to a DSA mechanism, although, as mentioned before, there are other

alternatives proposed lately. Only 2–8 % of clusters show radio shocks (Kale et al. 2015) and most of them are generally in or near the plane of the sky, which indicates a clear selection bias. Some of the radio shocks have associated X-ray shocks, usually found at the same location (see Table 1 of van Weeren et al. 2019). In some clusters two radio shocks appear diametrically with respect the center and are known as double shocks (i.e. double radio relics), such as Abell 3667 (Röttgering et al. 1997). Nowadays, a dozen of these systems have been discovered. The first radio shock detected was in the Coma cluster (Jaffe & Rudnick 1979; Ballarati et al. 1981). Afterwards, many others have been identified in the last years (for an extended list see Table 2 of van Weeren et al. 2019).

- **Revived AGN fossil plasma sources, phoenices, and GReETs**: These sources originate from the re-energisation of AGN fossil radio plasma in the ICM and are characterized by ultra-deep radio spectra. They are only visible in low-frequency radio observations.

  –*Revived AGN fossil plasma sources and radio phoenices*: They form by shock compression of old radio plasma. Phoenices (Kempner & David 2004) have irregular morphology, although the most common one is elongated and filamentary. The spectral index is α < -1.5. Compared with radio shocks they are located at smaller distances from the cluster center, they have smaller size ($\leq$ 300-400 kpc), lower polarization and radio power. The re-acceleration of the seed population in the ICM is thought to be the CR acceleration mechanism (Markevitch et al. 2005; Kang et al. 2012). Some of these sources have been found in e.g. Abell 1931 (Brüggen et al. 2018) and Abell 1914 (Mandal et al. 2019).

  –*GReETs*: Gently re-energized radio galaxy tails (De Gasperin et al. 2017), which present unexpected spectral flattening. It seems that the radiative losses of the CR are balanced with the particle re-energization, giving as a result the synchrotron spectrum flattening. Fermi-II processes are proposed for the particle re-acceleration mechanism. GReETs have been found in Abell 1033 (De Gasperin et al. 2017), Abell 1314 (Wilber et al. 2019) and ZwCl0634.1+4750 (Cuciti et al. 2018).

- **Radio halos**: Cluster-wide extended radio sources, which follow the ICM mass in the cluster center, do not present optical counterparts and there is no X-ray shock associated. The particle (re)acceleration is generated by means of the turbulence in the ICM via Fermi-II processes and/or secondary electrons. They include giant radio halos, mini-halos and "intermediate" halos, a possible transition or interface between the two previous categories (for a review, see Brunetti et al. 2001; Feretti et al. 2012; van Weeren et al. 2019).

  –*Giant radio halos*: Mpc-size radio sources found in massive dynamically disturbed clusters, usually as a consequence of a merger (Giovannini et al. 1999; Buote 2001; Cassano et al. 2010). They are found generally unpolarized. The typical spectral index varies between -1.4 < α < -1.1 (Giovannini et al. 2009). Different studies have shown that 60–80% with $M > 8 \times 10^{14}$ $M_{\odot}$ (20–30% below this mass) host giant radio halos. Nowadays, there are about 65 radio halos confirmed, e. g. Coma cluster (Large et al. 1959; Willson 1970), MACS J0717.5+3745 (Bonafede et al. 2009; van Weeren et al. 2009) or Abell 665 (Moffet & Birkinshaw 1989; Feretti et al. 2004b; Vacca et al. 2010).

–*Mini-halos*: They are found in the centers of relaxed CC clusters, often surrounded by cold fronts (Mazzotta & Giacintucci 2008). Their typical size is 100–500 kpc, similar to the extension of the central cooling regions around the BCG (for a review, see Gitti et al. 2015). The spectral index is similar to giant radio halos. Giacintucci et al. (2017) found that 80% of the CC clusters host mini-halos, while no evidence of them is found in NCC clusters. The Perseus cluster (Miley & Perola 1975; Pedlar et al. 1990) hosts a mini-halo as some other clusters such as e.g. Phoenix cluster (van Weeren et al. 2014) or RXJ1347.5-1145 (Gitti et al. 2007).

1.2.3 Comparison between X-ray and radio components of ICM shocks

As mentioned before, in some merging clusters both X-rays and radio emission are associated with the same shock. In 2010 Finoguenov et al. (2010) found the first evidence of X-ray and radio emission from the same shock in Abell 3667. Since then the number of discoveries have been increasing in the last decade (Macario et al. 2011; Ogrean & Brüggen 2013c; Bourdin et al. 2013; Eckert et al. 2016b; Sarazin et al. 2016; Akamatsu & Kawahara 2013a; Akamatsu et al. 2015, 2017; Botteon et al. 2016a,b; Urdampilleta et al. 2018; Di Gennaro et al. 2019).

The study of the radial distribution of these thermal and non-thermal components allows to determine the physical association between X-ray and radio emission from shocks as well as the thermodynamical properties and the dynamical state of the merging system. The comparison of Mach numbers derived from X-ray ($\mathcal{M}_X$) and radio ($\mathcal{M}_R$) observations can also reveal important information about the underlying assumptions, such as the particle acceleration mechanism. In the last years, discrepancies between both values have been found for most of the merging systems. The Mach number tends to be $\mathcal{M}_R > \mathcal{M}_X$ in most of the cases (see Table 2.10 and Fig. 2.16 in **Chapter 2**), except for the western shock of A3376 (see possible explanation in Section 2.4.4 of **Chapter 2**). It seems that $\mathcal{M}_X$ is somehow underestimated due to possible projection effects and/or the complexity of shock surface (Rajpurohit et al. 2018). Furthermore, recent radio observations have contributed to reduce the discrepancy. The low-frequency observations of LOFAR, for example, allow to determine with higher accuracy the injected spectral index (Hoang et al. 2017), therefore the $\mathcal{M}_R$. Akamatsu et al. (2017) discuss possible causes of this discrepancy (see their Section 4.3. for more details): (i) projection effects, (ii) Ion-electron non-equilibrium after shock heating, (iii) clumpiness and inhomogeneities in the ICM, (iv) a non-uniform Mach number or (v) pre-existing low-energy relativistic electrons and/or re-accelerated electrons, among others. A conclusive explanation of the Mach number difference is still far from being determined, but future X-ray observatories, such as *XRISM* and *Athena* will definitely shed further light on this issue (see Section 1.6).

1.3 Metal Enrichment in Galaxy Clusters

The hot plasma, ICM, is also known to be a rich archive of the past chemical history of the galaxy cluster. From the study of this enriched diffuse gas, crucial information over the galaxy cluster formation and evolution can be derived, such as merging and star-formation histories or stellar evolution. The heavy elements present in the ICM originate mainly from core-collapse (SNcc) and type Ia (SNIa) supernovae, which continuously release their nucleosynthesis products since the epoch of major star formation ($z \sim 2$–3) (Hopkins & Beacom 2006; Madau & Dickinson 2014). SNcc evolve from massive short-living stars and produce mainly oxygen (O) and other α-elements such as neon (Ne), magnesium (Mg), silicon (Si) and sulfur (S). On the other hand, SNIa emerge from the explosion of white dwarf stars in binary systems and contribute to increase the heavier metals such as argon (Ar), calcium (Ca), manganese (Mn), iron (Fe) and nickel (Ni). Finally, the bulk of carbon (C) and nitrogen (N) are mostly expelled by low-mass stars on the asymptotic giant branch (AGB). Recent studies (Ezer et al. 2017; Mernier et al. 2017; Mao et al. 2019) address that the ICM is enriched with a similar relative contribution of SNcc and SNIa products in all the cluster extension from the core to the most virialised regions. Once SN explosions or AGB stars release the metals, different physical and dynamical processes drive their distribution and mixing along the ICM, such as galactic winds (Kapferer et al. 2006, 2007; Baumgartner & Breitschwerdt 2009); ram-pressure stripping (Schindler et al. 2005; Kapferer et al. 2007), active galactic nucleus (AGN) outflows (Simionescu et al. 2008, 2009; Kapferer et al. 2009) or gas sloshing (Simionescu et al. 2010; Ghizzardi et al. 2014), among other processes. Detailed reviews on the observation of metals in the ICM include, e.g., Werner et al. (2008); Böhringer & Werner (2010); de Plaa (2013) and Mernier et al. (2018b).

In the last years, the spatial distribution of Fe in galaxy clusters has been extensively studied using the different X-ray observatories such as *ASCA*, *BeppoSAX*, *XMM-Newton*, *Chandra* or *Suzaku* (De Grandi & Molendi 2001; De Grandi et al. 2004; Baldi et al. 2007; Leccardi & Molendi 2008; Maughan et al. 2008; Matsushita 2011; Mernier et al. 2016, 2017; Mantz et al. 2017; Simionescu et al. 2017; Simionescu et al. 2019; Liu et al. 2018; Lovisari & Reiprich 2019). Most of the studies have been mainly devoted to the cool-core clusters except for the work by De Grandi et al. (2004) and Lovisari & Reiprich (2019), where an extended analysis for non-cool-core cluster is described. Previous analyses concluded that the radial distribution of Fe is centrally peaked for CC clusters, with a pronounced gradient up to $0.3 r_{500}$ and flattening for larger radii till a uniform value of $\sim$0.2–0.3 $Z_{\odot}$. The behavior of NCC clusters is clearly different (see Fig. 1.5). They show a flat distribution in the core, followed by a shallower gradient than the CC clusters, but with the same universal distribution for outer radii. The averaged Fe distribution of the recent study by Urdampilleta et al. (2019) (see **Chapter 4**) of six merging clusters show a good agreement with the radial distribution by Lovisari & Reiprich (2019) for NCC clusters. Moreover, X-ray observational studies (Ettori et al. 2015; McDonald et al. 2016; Mantz et al. 2017) and simulations (Biffi et al. 2017; Vogelsberger et al. 2018) suggest that the Fe abundance distribution and ICM metallicity remain nearly invariant within r_{500} between $z \sim 2$ and $z = 0$.

Nowadays, two possible scenarios for the metal enrichment in galaxy clusters are under debate:

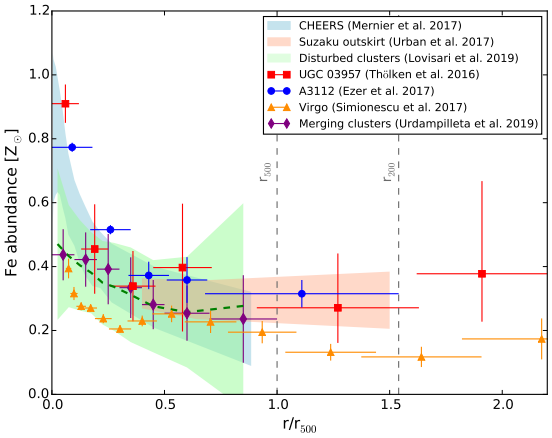

Figure 1.5: Measured radial Fe abundance profile in cool-core and non-cool-core clusters compiled from recent works. The blue, red and green shaded areas show respectively the CHEERS sample (Mernier et al. 2017), the 10 cluster outskirts sample (Urban et al. 2017) and disturbed clusters sample (Lovisari & Reiprich 2019). The CHEERS and *Suzaku* samples are stacked following the Mernier et al. (2017) method. The red squares, the blue circles, the orange triangles and purple diamonds show respectively the UGC 03957 group (Thölken et al. 2016a), the Abell 3112 cluster (Ezer et al. 2017), the Virgo cluster (Simionescu et al. 2017) and the merging clusters sample Urdampilleta et al. (2019). All the abundances are rescaled with respect to the proto-solar values of Lodders et al. (2009).

– Pre-enrichment scenario: Suggests that most of the metal enrichment of the ICM took place in the early stages of cluster formation (i.e. at $z > 2$–3; for recent reviews, see Mernier et al. 2018b; Biffi et al. 2018b). As a result, a uniform Fe abundance in the cluster outskirt is expected with a value around 0.2–0.3 $Z_{\odot}$.

– Late enrichment scenario: Proposes that the bulk of Fe was added at relatively recent times by merging or accretion processes, and mixed efficiently in the entire cluster volume. In this scenario, the Fe abundance at large radii in such dynamically disturbed systems would present notable gradients, with values higher than 0.2–0.3 $Z_{\odot}$.

As explained above, the CC and NCC profiles present similarities in the outskirts of the galaxy clusters, following a uniform radial distribution around 0.2–0.3 $Z_{\odot}$ (Fujita et al. 2008; Werner et al. 2013; Urban et al. 2017; Ezer et al. 2017; Simionescu et al. 2017). The simulations of Biffi et al. (2017) , Biffi et al. (2018a) and Vogelsberger et al. (2018) are able to reproduce the observables of the pre-enrichment scenario including in the physical processes of the stellar and AGN feedback. This means that the Fe distribution in cluster outskirts is independent of the dynamical state of the cluster, which together with the Fe abundance uniformity (0.2–0.3 $Z_{\odot}$) found, establish relevant additional evidence in favour of the pre-enrichment scenario.

1.4 Why X-ray spectroscopy

Many astrophysical sources in our Universe, in addition to galaxy clusters, contain X-ray emitting plasma, such as the coronae of cool stars, the winds of hotter stars, the hot component of the interstellar medium and the Warm-hot intergalactic medium (WHIM). Most of these plasmas are in collisional ionization equilibrium (CIE), where no external radiation field effects are present. Concretely, the ICM is mostly (excluding resonant scattering) an optical thin plasma which is in CIE and confined by the cluster gravitational potential well. Its spectrum contains two main components: one, the X-ray continuum emission mainly by bremsstrahlung, and further, the spectral emission lines. The continuum level can provide the temperature of the ICM and the equivalent width of the emission lines is proportional to the abundance of the metals that produce them (see Fig. 1.6). Apart from the temperature and abundances, X-ray spectra allow to obtain other physical properties such as densities, velocity field and ionization state as well. Therefore, X-ray spectroscopy is a crucial tool to infer the thermodynamical and chemical properties of the ICM.

One of the most significant contributions of X-ray spectroscopy to cluster science is the discovery of the "cooling flow problem". Following the classical cooling flow model the spectra of the cluster center should contain ions emitting at very low temperatures. On the contrary, no evidence of such emission lines was found by different X-ray observatories. Currently, as introduced in Section 1.1, it is thought that the cluster central cooling is balanced by (the) AGN feedback. In the case of merger shocks science, X-ray spectroscopy is decisive to determine the temperature and density of the post-shock and pre-shock regions, and therefore their discontinuities in the presence of the shock. Because shocks often occur at cluster outskirts, where the surface brightness is low, the shock detection can be challenging. Moreover, X-ray spectroscopy is also useful to determine the chemical enrichment in the ICM. The analysis of the emission lines associated with the metal production can reveal valuable information about the enrichment history.

Figure 1.6: *Left panel*: Ilustration of the *Suzaku* satellite. Credit: JAXA. *Middle panel*: Ilustration of the *XMM-Newton* satellite. Credit: ESA. *Right panel*: EPIC instrument (*XMM-Newton* satellite) spectra of the core region of the Abell 4059 cluster (Mernier et al. 2015).

Nowadays there are three methods to measure the X-ray spectra: CCDs, gratings and micro-calorimeters. CCDs are used for imaging observations with moderate field-of-view (FOV) and low/medium spectral resolution. The recent generation of X-ray satellites are

provided with this kind of detectors: the EPIC instrument in *XMM-Newton*, the ACIS instrument in *Chandra* and the XIS instrument in *Suzaku*. Gratings have higher spectral resolution but limited imaging capabilities. They are mainly devoted to point sources. *XMM-Newton* hosts the RGS instrument and *Chandra* the LETG and HETG spectrometers. Microcalorimeters are a recent development, that offer unprecedented high-resolution spectroscopy capabilities. The X-ray spectrometer of *Hitomi*, the Resolve instrument aboard *XRISM* and X-IFU aboard *Athena* are good examples of this kind of detectors.

1.5 Plasma codes for X-ray spectroscopy

Every spectrum containing spectral lines need spectral plasma codes to model and fit it. Atomic data are clearly needed for the interpretation of line fluxes, ratios and ionization states of the emitting plasma. Driven by the future high-resolution spectroscopy requirements (∼6-7 eV or ∼2.5 eV) of new X-ray satellites (i. e. *XRISM* or *Athena*), updates and improvements of the plasma codes are required. Some of the plasma codes for X-ray plasma spectra modeling, fitting and analysis available nowadays (for a review, see Kaastra et al. 2008) are SPEX[2] (Kaastra et al. 1996) , see more details in Section 1.5.1, AtomDB[3], with latest version v3.0.9 included in XSPEC (Arnaud 1996), and CHIANTI[4] (Landi et al. 2006), the latest version v9.0 (Del Zanna et al. 2015) . There also codes focusing on photoionised plasmas such as XSTAR[5] (Kallman & McCray 1982), current version 2.39, and Cloudy[6], with the latest version v17.01 (Ferland et al. 2017).

1.5.1 SPEX

The first work on X-ray spectra modelling at SRON started in the late 1960s and the first code was initially written by Mewe (1972). After some updates (Mewe et al. 1985, 1986), this plasma code became a reference for many years. The code was later updated first as the MEKA (following its main contributors: Rolf Mewe and Jelle Kaastra), and then as MEKAL code in 1995. It was incorporated into the XSPEC fitting package (Arnaud 1996). In 1991 the MEKAL code evolved into the SPEX package and around 1996 the second version v2.0 was developed (Kaastra et al. 1996), driven by the preparation for the *Chandra* and *XMM-Newton* satellites launched in 1999. In 2016 high-resolution spectroscopy observations were expected from the *Hitomi* satellite and most of the plasma codes were considerably updated for the occasion (Hitomi Collaboration et al. 2018a). For this same reason, in January 2016, SPEX v3.0 (Kaastra et al. 2017b) was released. This version aimed to follow the original strategy of Mewe (1972), which is minimizing the number of mathematical operations and data storage to achieve simple and fast, but accurate calculations. A comparison of the Fe abundance for the CHEERS sample using SPEX v2.0 vs. v3.0 can be seen in Mernier et al. (2018a). Currently the latest version is 3.05.00, see the description

[2] https://www.sron.nl/astrophysics-spex
[3] http://www.atomdb.org/
[4] http://www.chiantidatabase.org/
[5] https://heasarc.gsfc.nasa.gov/lheasoft/xstar/xstar.html
[6] https://www.nublado.org/

in the SPEX Manual[7] from December 2018. One of the new updates in SPEX v3.0 was the new atomic database prepared mainly by Ton Raassen, which includes thousands of lines and transitions from hydrogen to zinc, obtained from the literature or calculation made with FAC (Flexible Atomic Code, Gu 2002), and is part of the SPEXACT (SPEX Atomic Code and Tables). The other updates were related to the following radiative processes (Kaastra et al. 2008, 2017c):

- **Radiative recombination (RR)** is the reverse process of photoionization. A free electron is captured by an ion while emitting a photon, it is also known as free-bound continuum emission. The update of RR data for SPEX v3.0 include the parameterization of the most recent calculations done by Mao & Kaastra (2016) and Mao et al. (2017).
- **Collisional ionization (CI)** occurs during the interaction of a free electron with an atom or ion. The free electron transfers a part of its energy to one of the bound electrons and this is able to escape from the ion (Direct Ionization, DI). Another intermediate ionization process can happen called Excitation-Autoionization (EA). If the free electron has insufficient energy to ionize the ion directly, the collision can bring one of the bound electrons in a higher shell by excitation. The ion will return to its ground level by a radiationless autoionization transition, which causes the liberation of the previously excited electron (see Fig. 1.7). The inner-shell ionization data for CI and EA have been updated in SPEX v3.0 including the new laboratory measurements and theoretical calculations of the CI cross-sections (Urdampilleta et al. 2017, see **Chapter 5**).

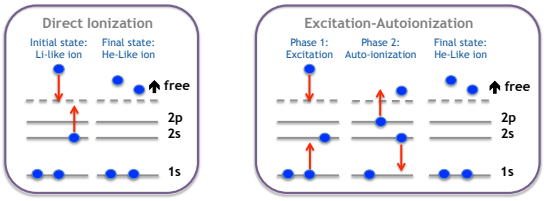

Figure 1.7: Direct Ionization and Excitation-Autoionization of Li-like ion.

- **Charge exchange (CX)** occurs when an ion collides with a neutral atom, and catches an electron from the atom. The captured electron often relaxes down to the ground via line emission. A new CX model has been incorporated in SPEX v3.0 (Gu et al. 2016).
- **The Photoionization** process is similar to CI but with a photon instead of free electron causing the ionization. It takes place during the interaction of a photon with an atom or ion, the photon transfers a part of its energy to one of the bound electrons, which is able to escape from the ion. Updates in the PION model of SPEX that models a photoionized plasma and a comparison with other photoionization codes are described in Mehdipour et al. (2016).

[7] https://www.sron.nl/astrophysics-spex/manual

1.6 Future prospects

Since the 80s, different X-ray observatories (*Einstein*, *EXOSAT*, *ROSAT*, *ASCA*, *BeppoSAX*, *XMM-Newton*, *Chandra*, *Suzaku* and *Astrosat*) have allowed to extensively analyze the gas density, temperature and abundance distribution in galaxy clusters. However, the key improvement came with upgraded spectroscopic and imaging capabilities of the most recent X-ray satellites such as *XMM-Newton*, *Chandra* and *Suzaku*. The first two were launched in 1999 and they are still operative, while *Suzaku* finished its operational lifetime in 2015. *Chandra* has a high angular resolution (i.e. $1''$ at $z < 0.05$ corresponds to < 1 kpc, Markevitch & Vikhlinin 2007), which can provide detailed images of the ICM substructures such as shocks or cold fronts produced as a consequence of gas sloshing, subcluster accretion or merging, among other processes. *XMM-Newton*, in spite of having a moderate angular resolution, is not sufficient to visualized these features, but it can determine the ICM temperature and measure abundances with higher statistical accuracy due to its larger effective area and spectral resolution. On the other hand, the strength of the *Suzaku* satellite was its low instrumental background and stable detectors, which allowed to observe the low surface brightness regions, e. g. cluster outskirts, where usually X-ray shocks are located.

In the last few decades, our understanding of the astrophysics and evolution of galaxy clusters has considerably improved thanks to the previously mentioned X-ray observatories. Nevertheless, some fundamental questions, related to the science topic of this thesis, remain still open such as: (i) how do hot diffuse baryons accrete and dynamically evolve in the dark matter halos? and (ii) what drives the chemical and thermodynamic evolution of galaxy clusters? (Ettori et al. 2013; Guainazzi & Tashiro 2018). The next generation of X-ray missions will address all these open questions. We have already glimpsed the power of micro-calorimeter detectors through the *Hitomi* satellite (Section 1.6.1). In Section 1.6.2 and 1.6.3, the highlights of these exciting missions, *XRISM* and *Athena*, are described respectively.

1.6.1 Hitomi

Hitomi, the Japanese satellite, was successfully launched on 17th February 2016. Unfortunately, during the commissioning phase, one month after the launch, the satellite broke away as a result of several failures in the attitude and orbital control subsystem. On 28th April 2016 JAXA declared the mission officially finalized. *Hitomi* was provided with two soft X-ray telescopes, a soft X-ray imager (SXI) and a soft X-ray spectrometer (SXS), a micro-calorimeter instrument, in addition to two gamma-ray detectors. SXS had a FOV of $3' \times 3'$, with a high energy resolution of $\sim$5 eV in the 0.4–12 keV band, allowing to do high-resolution spectroscopy at an unprecedented level (see the spectrum of the Perseus galaxy cluster in Fig. 1.8).

Before the satellite failure, *Hitomi* was able to observe the Perseus galaxy cluster. The high-resolution of the SXS instrument allowed to measure the detailed structure of spatially resolved emission lines, the velocities of gas motions, metallicities and the multi-temperature structure of the gas in the core of the Perseus cluster (Hitomi Collaboration

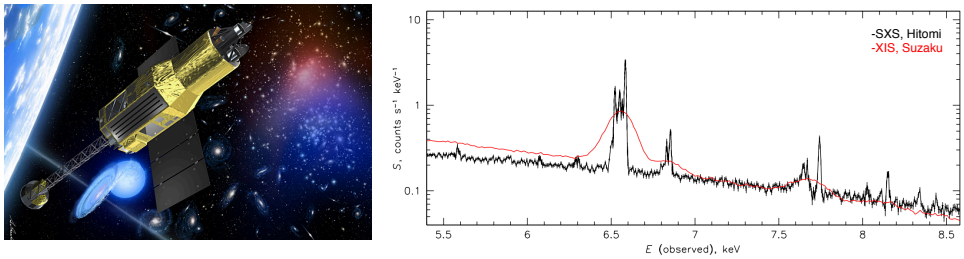

Figure 1.8: *Left panel*: Ilustration of the *Hitomi* satellite. Credit: JAXA. *Right panel*: SXS (*Hitomi*) spectrum of the full field overlaid with a CCD (*Suzaku*) spectrum of the same region of Perseus galaxy cluster. Credit: Hitomi Collaboration et al. (2016).

et al. 2018b,c,d; Simionescu et al. 2019). This observation, accomplished with the gate valve closed (not fully operative), revealed a very high resolution spectrum using the micro-calorimeters. This showed the first realistic proof of the high potential of this kind of detectors, which open a new window on the merging galaxy clusters and the ICM chemical enrichment studies.

1.6.2 XRISM

Based on the extraordinary performance and results obtained from the Perseus cluster, the only available cluster observation, by the *Hitomi* satellite, JAXA and NAXA decided to propose a recovery mission expected to be launched in early 2022. It has been recently renamed as *XRISM* (X-Ray Imaging and Spectroscopy Mision) (Tashiro et al. 2018). There will be two instruments on board XRISM: a soft X-ray micro-calorimeter (Resolve) with an energy resolution of $\leq$ 7 eV in the 0.3–12 keV range and a FOV of $3' \times 3'$, and an array of CCD detectors (Extent) with an energy resolution of $\sim$170 eV @ 6 keV and a larger FOV > $30' \times 30'$. Both instruments have similar characteristics to the SXS and SXI instruments of *Hitomi*. The main advantages of *XRISM* are the high spectral resolution provided by the micro-calorimeter and the low instrumental background level, seven times lower than *Suzaku*. The high resolution will allow to measure with higher accuracy the metal abundances in galaxy clusters such as O, Ne and Mg, to fully resolve all the Ni and Fe lines and to disentangle rare elements as Na or Al. The low background makes *XRISM* one of the most suitable satellite to observe low-count-rate regions at cluster peripheries and to look for accretion and merger X-ray shocks.

1.6.3 Athena

Athena is the second L-mission of the ESA "Cosmic Vision" program to be launched around 2030. *Athena* aims to address the science topics of the "Hot and Energetic Universe" (Nandra et al. 2013). The instruments on board are the X-ray Integral Field Unit (X-IFU, Barret et al. 2018), a cryogenic imaging spectrometer with a 2.5 eV energy resolution in the 0.2–12 keV band and a FOV of $5' \times 5'$, and the Wide Field Imager (WFI, Meidinger et al. 2018), a

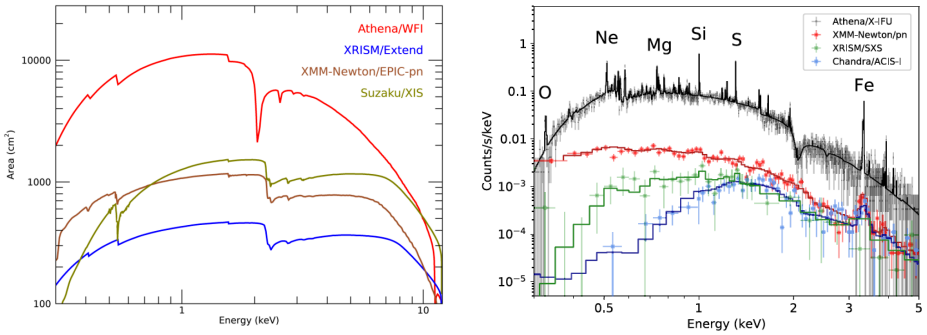

Figure 1.9: *Left panel*: Effective area comparison of CCD detectors. Credit: Mateo Guainazzi, ESA. *Right panel*: Simulated 250 ks spectrum of the core of a galaxy cluster (kT = 3 keV, z = 1) for the *Athena* X-IFU instrument, *XMM-Newton* pn, *XRISM* SXS and Chandra ACIS-I. Credit: Mernier et al. (2018b).

DEPFET detector with a wide FOV (40′×40′) and moderate energy resolution (≤150 eV @ 6 keV). The revolutionary capabilities of *Athena* are focused on its effective area, which is considerably larger than previous satellites (see left panel of Fig. 1.9) and the high spectral resolution of 2.5 eV over a broad energy band. The combination of these performances will enable a definitive understanding of merger X-ray shock physical properties and their role in the evolution of large-scale cosmic structure. For example, *Athena* will allow to obtain an accurate temperature structure map of the post and pre-shock regions, rising possible substructures and reconstructing the original temperature structure. Moreover, the measurement of the ion temperature via the thermal broadening of the emission line will be possible, similar to the diagnostic of the non-Maxwellian tails of the electron distribution (Kaastra et al. 2009). Finally, more accurate temperature and density discontinuities characterization will be obtained in shock regions, providing a better comparison with radio observations, and therefore better understanding of the particle acceleration mechanism.

The chemical enrichment science will benefit from the high spectral and spatial resolution to provide unprecedented accurate abundance measurements, not only the better characterized elements but also the new ones such as Cr, Mn, N or Na (see right panel Fig. 1.9). This will provide better constrains for the metal production mechanisms via SN and AGBs. Moreover, detailed metal distribution maps will be derived, as well as the metal radial distribution for radii larger than r_{500}. For the first time the abundances at the cluster outskirts and beyond will be estimated, which will shed light on the cluster enrichment scenario.

1.7 Thesis outline

This thesis focuses on the X-ray spectral analysis of merging galaxy clusters and the plasma code development for future high-resolution X-ray spectroscopy observations. This work deepens in two different aspects of these merging clusters still under debate: one, the study of the thermal (X-ray shocks) component and its correlation with the non-thermal

(radio shocks/relics) component, and two, their metal enrichment history. The first one is crucial to understand how the shocks propagate and heat the ICM as well as to determine the physical association between these two components. The second one aims to contribute to a better knowledge of the metals origin, evolution and distribution in merging clusters, which can reveal important information on the dynamical history of the mergers.

Chapter 2

In Chapter 2, we investigate the spatial distribution of X-ray shock structures of the merging galaxy cluster Abell 3376 and study their relation with the radio shocks (relics). We analyze *Suzaku* observations, which cover the entire double radio relic region (Mpc-size) in the cluster outskirts. We determine the radial temperature profiles in four different directions: west, east, north and south. All of them except the south show evidence of a deviation from the universal temperature profile of relaxed clusters, suggesting a possible presence of X-ray shocks. However, we find a clear temperature jump and density discontinuity derived from the surface brightness using *XMM-Newton* observations, only in the west and east. We confirm that one X-ray shock is located at the western radio relic and another one probably associated to the 'notch' of the eastern relic. Moreover, we detect a cold front at the east using a *Chandra* observation. The Mach numbers derived from radio observations are consistent with the Mach number derived from X-rays in the eastern shock, but slightly lower for the western one, probably due to the radio ageing effects. Finally, we estimate that the merger is taking place close to the plane of the sky and the dynamical age is ∼0.6 Gyr after core passage, indicating that Abell 3376 is a young merger, still evolving.

Chapter 3

In Chapter 3, we show the spectral analysis of the multi-merging galaxy cluster Abell 3365 observed with *XMM-Newton* satellite. In our study we find two strong X-ray shocks with a $\mathcal{M} > 3$, co-located with a western radio relic and eastern radio relic candidate, based on the temperature discontinuity. We also observe a cold front at the west of the X-ray emission peak, which delimit a very high abundance gas (∼0.6 $Z_{\odot}$), displaced from the central potential well due to dynamical internal force of the cold front. In addition we determine the radial temperature, abundance and pseudo-entropy distribution along the merging axis of the disturbed intra-cluster medium. Finally, we calculate the shock acceleration efficiency at the eastern radio relic, which suggest that the DSA scenario is a possible acceleration mechanism for shocks with $\mathcal{M} \gtrsim 3$.

Chapter 4

In Chapter 4, we present an iron abundance study for merging galaxy clusters using *XMM-Newton* observations. For the first time the temperature, abundance and pseudo-entropy distribution along the merging axis of six well known merging clusters (CIZA J2242.8+5301, 1RXS J0603.3+4214, Abell 3376, Abell 3667, Abell 665 and Abell 2256) are obtained up to r_{500}. The averaged Fe distribution shows a good agreement with NCC or disturbed clusters distribution. It has a moderate central peak, lower than CC or relaxed clusters, and flattens

for large radii towards a similar uniform distribution with a value $\sim$0.2–0.3 $Z_\odot$. Moreover, we find a mild correlation between abundance and psuedo-entropy in the central regions, while no evidence of the correlation is found in the cluster outskirts. This finding together with the abundance uniformity at large radii is valuable additional evidence in favour of the pre-enrichment scenario, which is found to be independent of the dynamical state of the cluster.

Chapter 5

In Chapter 5, we review the new laboratory measurements and theoretical calculations of single ionization cross sections available for ions from H to Zn. As a result of this work, we include in total 45 new data sets for different ions, while the rest of the ions are interpolated or extrapolated. We obtain not only the total cross sections, but all the inner shells cross-sections of the Direct Ionization (DI) and Excitation-Autoionization (EA) processes. We model and fit these processes using an extension of Younger's and Mewe's formula for DI and EA, respectively. The integration of these models over a Maxwellian velocity distribution allow us to derive the subshell ionization rate coefficients, which have been incorporated into the new version of SPEX v3.0.

"Take your passion
And make it happen
Pictures come alive
You can dance right through your life"

- Irene Cara, *Flashdance*